

# Synthesis of Hierarchical Bio-Inspired Pine Needle-Shaped MnO<sub>2</sub>/CNTs/Carbon Cloth Composite as Highly Cycling Stable Symmetrical Supercapacitor

Yunyu Li<sup>1,\*</sup>, Yi Liu<sup>1</sup>, Lingjun Guo<sup>2</sup>, Xianglin Ji<sup>2</sup>, Chuanyin Xiong<sup>2</sup>, Zhigang Zhao<sup>2</sup>, Qiang Song<sup>2,\*</sup>

<sup>1</sup> Xi'an Polytechnic University, Xi'an 710048, P R China

<sup>2</sup> Research Center of Carbon/Carbon Composites, State Key Laboratory of Solidification Processing, Northwestern Polytechnical University, Xi'an 710072, P R China

\*E-mail: [liyunyu@mail.nwpu.edu.cn](mailto:liyunyu@mail.nwpu.edu.cn), [songqiang511@nwpu.edu.cn](mailto:songqiang511@nwpu.edu.cn)

Received: 15 February 2017 / Accepted: 29 March 2017 / Published: 12 May 2017

---

In this work, bio-inspired hierarchical pine needle-shaped MnO<sub>2</sub>-CNTs-CFC composite was prepared by an environmentally-friendly two-step electrophoretic deposition (EPD) method. The synthesis of MnO<sub>2</sub> on CNTs was inspired by the “pine needle”. The nanostructured needle-shaped MnO<sub>2</sub> which is more resistant than that larger MnO<sub>2</sub> structures to fracture, due to no sufficient initiate crack propagation for the total elastic energy stored in a small nanostructure during deformation, which would effectively enhance the cycling stability. The CNTs serve as substrate providing a conductive channel for MnO<sub>2</sub> to harvest and store the charge. The large quantity of CNTs on the surface of carbon cloth may facilitate the loading of Pine needle-shaped MnO<sub>2</sub>, providing high speed channels for the charge carrier and pseudocapacitance. The electrochemical results show specific capacitance of 381.74 F·g<sup>-1</sup>, the energy density of 35.6 Wh·kg<sup>-1</sup> at a scan of 1 mV·s<sup>-1</sup> and capacitance retention ratio of 85% at a scan of 500 mV·s<sup>-1</sup>. The capacitance retention ratios of the flexible MnO<sub>2</sub>-CNTs-CFC hybrid are no less than 75% when they endure various mechanical deformations. The flexible supercapacitor is obtained with promising electrochemical properties and rosy flexibility, demonstrating its great potential for wearable storage devices.

---

**Keywords:** Flexible super-capacitors; Bio-inspired; Electrophoretic deposition; MnO<sub>2</sub>

## 1. INTRODUCTION

Supercapacitor has been developed to satisfy future societal and environmental needs [1-4] due to its high power density, long cycle life, short response time and good durability. Supercapacitor making them readily to integration into commercial products is demand of novel specifications, for example, wearable energy storage devices [5-8]. The wearable supercapacitor device needs not only

higher capacity in function but also lightweight, softness, flexibility, and stylish in various service conditions [9-13]. However, aforementioned performances are far less satisfactory, which limits supercapacitor's applications. In order to break through these limitations, materials with both high energy densities, excellent mechanical flexibility and longer cycle life properties are urgently in need. Aiming for this, tremendous efforts have been carried out, especially in the textile-based energy storage devices [8-13, 14]. Recently, the emerging intelligent textiles with electronics, such as yarns [12-13], fabrics [11-12], and garments, were regarded as the ideal textile supercapacitors [5, 10-13]. Due to their textile-based flexibility, some potential advantages to wearable, comfort, convenience and fashion were emphasized. Unfortunately, for its widely applications, the textiles electrochemistry performances and the corresponding commercial fabricating difficulties are significant technical challenges [5]. Hence, by modifying electrochemical functionalities of the textiles, the high energy density and long cycling life can be obtained [15].

CNTs have aroused great interests as a kind of carbon electrode material due to their unique structural properties, significantly high electrical and thermal conductivity, great mechanical strength and high surface area [16, 17].  $\text{MnO}_2$ , as a traditional pseudocapacitance material, has the advantage of low cost and exhibits high theoretical capacitance, good cycle stability, and eco-friendliness [18-21]. The CNTs and  $\text{MnO}_2$ , with special bio-inspired needle-shaped structure, combining with the flexible structure of CFC, may receive better capacitance performances to overcome the difficulties on textiles electrochemistry performances. The combination was mainly using EPD, which is a facile and mild method with low-energy and the outstanding ability to homogeneously coat flexible textiles with films of controlled thickness and density during process of material fabrication [4, 22-26], compared with the conventional method [27-28].

In this context, bio-inspired hierarchical pine needle-shaped  $\text{MnO}_2$ -CNTs-CFC composite was prepared by an environmentally-friendly two-step electrophoretic deposition (EPD) method. The synthesis of  $\text{MnO}_2$  on CNTs was inspired by the "pine needle". The needle shape  $\text{MnO}_2$  with nanoscale effect could ease the volume expansion effect and effectively enhance the cycling stability. The CNTs serve as substrate providing a conductive channel for  $\text{MnO}_2$  to harvest and store the charge. The large quantity of CNTs on the surface of carbon cloth facilitates the loading of pine needle-shaped  $\text{MnO}_2$ , providing high speed channels for charge carrier and pseudocapacitance.

## 2. EXPERIMENTAL

### 2.1. Deposition of CNTs on CFC

For starter, 1K plain CFC (warp and weft used T300-1K yarn, and thickness was 0.15 mm, Jiangsu Tianniao High Technology Co. Ltd., China) with a weight of  $119 \text{ g}\cdot\text{m}^{-2}$ , were used as the substrate materials. Secondly, a porous carbon CNTs network was coated on the CFC by one-step EPD. CNTs paste, 9.6 wt.% multi-walled CNTs ranging from 20 to 40 nm and with the length of 30  $\mu\text{m}$  (Chengdu, Timesnano, China) was dispersed in isopropyl alcohol for 3 h ultrasonic process to get suspension of  $1.0 \text{ g}\cdot\text{L}^{-1}$ . The CFC connected with a copper wire as a cathode was fixed in a plastic

frame, then was immersed in an EPD cell containing stable CNTs suspension. A stainless steel plate was placed on the opposite side as an anode. The experiment with a PowerPac Basic (Bio-Rad Laboratories, Inc., USA) was performed at a constant voltage of 40 V and an electrode distance of 10 mm. EPD time was 60 s. The samples were dried in a vacuum drying chamber for 2 h at 60 °C.

## 2.2. Fabrication of pine needle-shaped $\text{MnO}_2$

The pine needle-shaped  $\text{MnO}_2$  was synthesised in a mixed solution of manganese acetate and sodium sulfate in deionized water (both were 0.15 M) via EPD again using CNTs/CFC as substrate. The  $\text{MnO}_2$ -CNTs-CFC hybrid and  $\text{MnO}_2$ -CNTs (nano) structure were successfully synthesized by a cathode EPD. The main EPD parameters were the electrode distance (10 mm), the time (7 min) and the deposition voltage from 3.0 to 7.0 V (3.0, 4.0, 5.0, and 7.0 V). Fig. 1 shows the synthetic procedures of the 3D  $\text{MnO}_2$ -CNTs-CFC hybrid composite. The pine needle-shaped structure of  $\text{MnO}_2$  was shown in SEM of Fig. 1.  $\text{MnO}_2$  as the pine grows on the branches of CNTs and the carbon fibers serve as tree trunks. The CNTs serve as substrate providing a conductive channel for  $\text{MnO}_2$  to harvest and store the charge. In this bio-inspired system, high electrical conductivity was providing according to the conducting vessel. The needle shape with nanoscale effect could ease the volume expansion effect and effectively enhance the cycling stability.

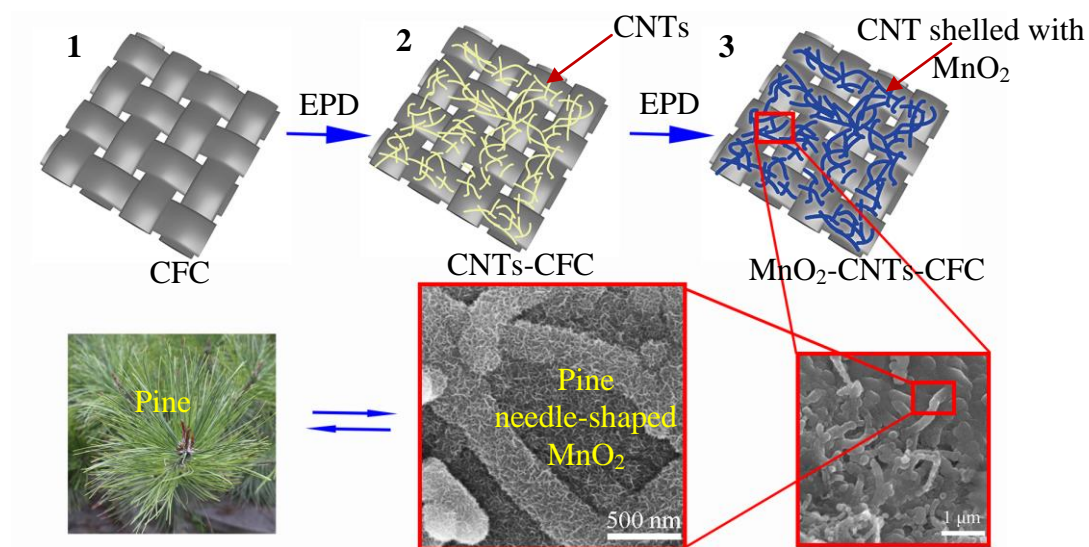


**Figure 1.** Scheme for the synthesis of the 3D  $\text{MnO}_2$ -CNTs -CFC hybrid composite.

## 2.3. Materials characterization

The morphology and microstructure of as-fabricated samples were investigated by scanning electron microscopy (SEM; FEI NANO450). The phase structure and structure information of as-prepared samples were characterized using X-ray diffraction (XRD, PANalytical X'Per PRO) and Raman Spectrometer (Renishaw in Via).

#### 2.4. Materials electrochemical test

The electrochemical behavior was analyzed by an electrochemical workstation (CHI 660D, Shanghai, Chenhua) in two electrode systems, where the samples were directly served as a working electrode and a counter electrode without binder separated by a middle diaphragm. Cyclic voltammograms (CV) measurements were conducted at scanning speeds ranging from 1 to 500  $\text{mV}\cdot\text{s}^{-1}$  in an electrolyte containing 6 M KOH at room temperature. The galvanostatic cycling for the electrode materials were tested at a current density of ranging from 0.1 to 3.0  $\text{A}\cdot\text{g}^{-1}$ . Electrochemical impedance spectroscopy (EIS) was carried out over a frequency range of 0.01 Hz to 100 kHz at open circuit potential with an ac perturbation of 10 mV. Specific capacitance  $C_m$  ( $\text{F}\cdot\text{g}^{-1}$ ), energy density  $W$  ( $\text{Wh}\cdot\text{kg}^{-1}$ ) and power density  $P$  ( $\text{kW}\cdot\text{kg}^{-1}$ ) were calculated from CV curves according to the equations as follows [29, 30]:

$$C_m = \int_{v_1}^{v_2} |I| dV / 2mv \Delta V \quad (1)$$

$$W = C_m V^2 / 2 \quad (2)$$

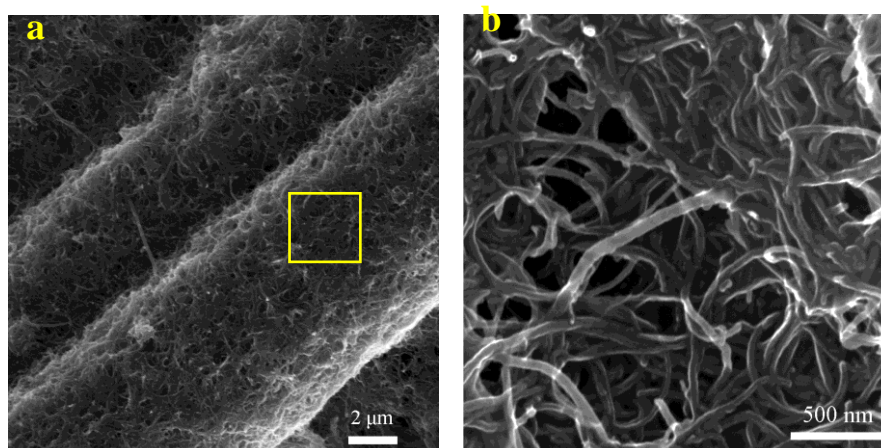
$$P = W / \Delta t \quad (3)$$

where  $I$  is the charge-discharge current,  $m$  is the total mass of  $\text{MnO}_2$ -CNTs in two electrodes,  $\Delta t$  is the discharge time, and  $\Delta V$  is the potential window during the CV measurements process.

### 3. RESULTS AND DISCUSSION

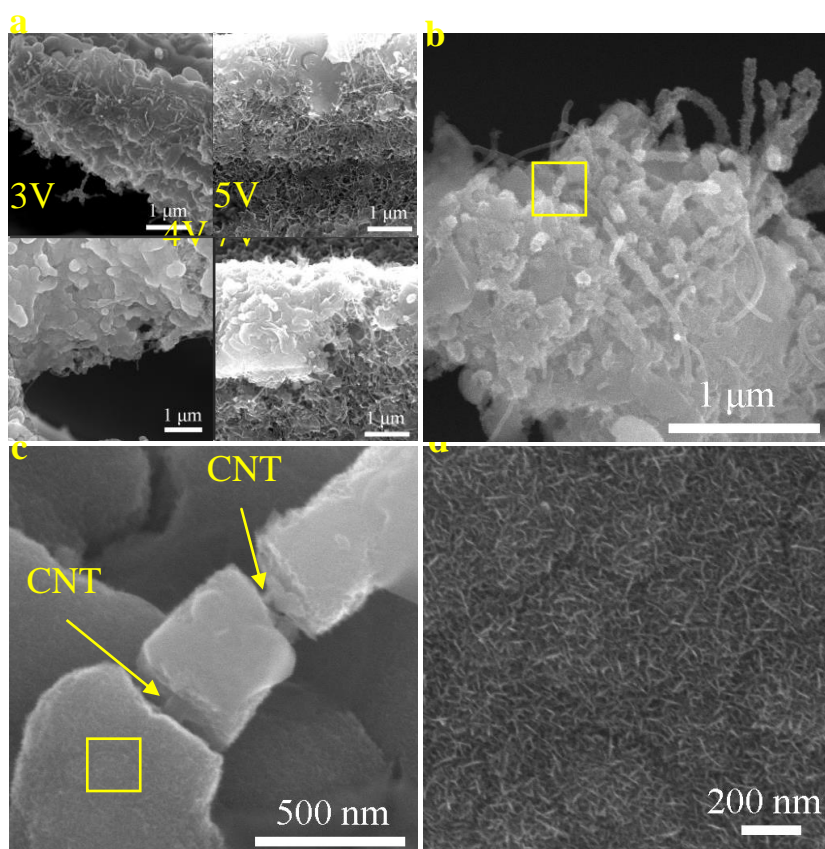
#### 3.1 Morphology and microstructure

Fig. 2a showed SEM images of CNTs-CFC hybrid by EPD. It can be observed that CNTs were deposited uniformly on the surface of carbon fibers without agglomerations and exfoliations. Fig. 2b shows SEM images of morphology and structure of deposited CNTs. The CNTs arranged randomly forming 3D network with some pores. These pores with a larger area could be filled by  $\text{MnO}_2$  via EPD processes to produce more available capacitance.



**Figure 2.** SEM images of (a) CNTs-CFC hybrid by EPD; (b) high magnification of CNTs in the dotted bordered rectangle of (a).

Fig. 3a shows images of MnO<sub>2</sub>-CNTs-CFC hybrid fabricated at different EPD voltages. The dense hierarchical structure of the MnO<sub>2</sub>-CNTs-CFC hybrid was obtained at 4V, and a mass of the pores blocked off without sufficient MnO<sub>2</sub> were empty at 7V. Moreover, the MnO<sub>2</sub> layers on the surface of network became thickening along with the increasing voltage (Fig. 3a) and apparent cracks were found while altering the voltage to 7V. Hierarchical uniform structures of the MnO<sub>2</sub>-CNTs-CFC hybrid with the cross-section of the network (Fig. 3b) were obtained when demonstrating well the power of 4V. In addition, the typical core-shell shape structure of CNTs-MnO<sub>2</sub> was found in Fig. 3c. The block of MnO<sub>2</sub> was mainly the agglomeration of the nano needle (Fig. 3d).



**Figure 3.** SEM images of MnO<sub>2</sub>-CNTs-CFC hybrid fabricated at different EPD voltage (b) MnO<sub>2</sub>-CNTs-CFC hybrid on the cross-section (c) magnification of CNTs-MnO<sub>2</sub> core-shell shaped in the dotted bordered rectangle of (b) and (d) magnification of MnO<sub>2</sub> array in the dotted bordered rectangle of (c).

Fig. 4a shows the as-fabricated hybrid XRD pattern. The diffraction peaks of MnO<sub>2</sub>-CNTs-CFC hybrid at 36.5° and 65.7° matched with the standard XRD pattern of birnessite-type MnO<sub>2</sub> [31]. A characteristic peak of CNTs-CFC hybrid at roughly 25.9° was consistent with C (002), which implied that the characteristic peak has shifted to right after the CNTs deposited onto the surface of CFC due to the better crystallization degree of CNTs. For comparison, a significant broadening peak of original CFC at 25.5° implies the mass of disordered crystal structure of graphite [32]. Fig. 4b shows the structural features of CFC, CNTs-CFC hybrid and MnO<sub>2</sub>-CNTs-CFC hybrid. The value of I<sub>D</sub>/I<sub>G</sub>

shifts to 0.64 in the CNTs-CFC hybrid due to the fewer defects of CNTs, for comparison, D and G bands of original CFC were inconspicuous. The Raman spectrum of the MnO<sub>2</sub>-CNTs-CFC hybrid matched at 643 cm<sup>-1</sup> which are the major vibrational features of the birnessite-type MnO<sub>2</sub> [33, 34]. There was reduced signal measured at located D and G bands, which indicated that hierarchical pine needle-shaped MnO<sub>2</sub>-CNTs. Consequently, the result was in good agreement with investigation of SEM (Fig. 3b, 3c and 3d).

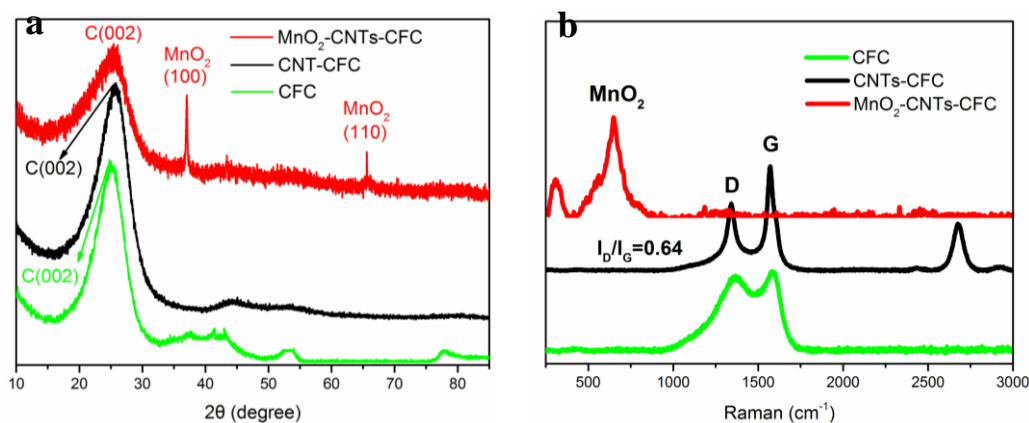


**Figure 4.** (a) XRD patterns of the CFC, CNTs-CFC hybrid and MnO<sub>2</sub>-CNTs-CFC hybrid (b) Raman spectrum of the CFC, CNTs-CFC hybrid and MnO<sub>2</sub>-CNTs-CFC hybrid.

### 3.2 Electrochemical performance

In order to reveal the capacitive performance, the MnO<sub>2</sub>-CNTs-CFC and CNTs-CFC hybrid have been directly used as binder-free working electrodes in 6 M KOH. The CV curves are usually used to characterize the electrochemical performance of the samples.[35, 36] The CV in Fig. 5a shows the CV curves of the MnO<sub>2</sub>-CNTs-CFC and CNTs-CFC hybrid at the scan rate of 50 mV·s<sup>-1</sup>. The absolute area of the CV curves of CNTs-CFC composite was obviously much more smaller than that of the MnO<sub>2</sub>-CNTs-CFC hybrid, demonstrating that the higher specific capacitance of MnO<sub>2</sub>-CNTs-CFC hybrid. This phenomenon was mainly attributed to the tree system of hierarchical MnO<sub>2</sub>-CNTs-CFC network with larger specific area. What's more, MnO<sub>2</sub> provided additional pseudocapacitance. The CV curves of the MnO<sub>2</sub>-CNTs-CFC at various scan rates ranging from 1 mV·s<sup>-1</sup> to 500 mV·s<sup>-1</sup> are displayed in Fig. 5b. The calculated specific capacitance values of the MnO<sub>2</sub>-CNTs-CFC hybrid were 381.74, 290.11, 192.62, 165.43, 130.07, 79.28 F·g<sup>-1</sup> in 1, 10, 20, 50, 100, 500 mV·s<sup>-1</sup>, respectively. The rectangular and symmetric shape was maintained when scan rates grow. Even up to 500 mV·s<sup>-1</sup>, the specific capacitance was calculated to be 79.28 F·g<sup>-1</sup> while the shape of the CV curve possessed no obvious changes, which might be to the result of the fast electrons and ions diffusion rate in the MnO<sub>2</sub>-CNTs-CFC electrode, where CNTs increase the electrical conductivity like pine branches-the electronic conductive channels (Fig. 1). Fig. 5c shows the galvanostatic charging-discharging (GCD) curves of MnO<sub>2</sub>-CNTs-CFC and CNTs-CFC electrode with a current density of 3.0 A·g<sup>-1</sup>. The discharging time of MnO<sub>2</sub>-CNTs-CFC electrode indicates that the capacitance difference would be

larger than that of CNTs-CFC electrode if  $\text{MnO}_2$  was loaded by appropriate EPD voltages. Moreover, the GCD curves showed a small IR decrease once discharging began, owing to the internal resistance between  $\text{MnO}_2$  and CNTs, CFC [26]. To improve hampered transmission of electrons, the 3D stable structure was obtained to form stereoscopic electronic transmission paths and increase more area for the  $\text{MnO}_2$  load (Fig. 2 and Fig. 3b), while  $\text{MnO}_2$  distributed on CNTs uniformly in determining the proper parameter for EPD (Fig. 3d). Thereafter, the improved curve of  $\text{MnO}_2$ -CNTs-CFC electrode with a less-obvious IR drop at the different current density indicated a rapid I-V response and a superior electrochemical reversibility as shown in Fig. 5d. The high energy density of  $35.6 \text{ Wh}\cdot\text{kg}^{-1}$ , while power density of  $9.2 \text{ kW}\cdot\text{kg}^{-1}$  was presented at the scan rate of  $1 \text{ mV}\cdot\text{kg}^{-1}$ .

What's most crucial was that the excellent conductivity of the trees system with the large specific area would provide a fast channel and large surface area for electronic transmissions. Furthermore, the enormous pseudocapacitance effect of pine needle-shaped  $\text{MnO}_2$  also contributes to the specific capacitance. In order to further study the structural and electrochemical characteristics of the as-fabricated hybrid, the EIS measurements were conducted with a frequency range from 100 kHz to 0.01 Hz, as shown in Fig. 5e. The straight line at low frequency, the slope of  $45^\circ$  portions of the curve at low frequency, and semicircle at high frequency were included in the Nyquist plots. The observed Nyquist plots which showed the presence of constant phase element ( $\text{CPE}_1$  and  $\text{CPE}_2$ ) involving the double layer and pseudocapacitance, solution resistance ( $R_s$ ), Warburg impedance ( $Z_w$ ) and charge-transfer resistance ( $R_{CT}$ ) [34]. The electrodes exhibited a low solution resistance ( $R_s$ ) with a presence of small semicircle region with a charge transfer resistance ( $R_{CT}$ ) of about  $0.04 \Omega$  between the electrode and electrolyte [35,36,37-39]. In the low-frequency region, the  $\text{MnO}_2$ -CNTs-CFC displays a near curve to CNTs-CFC, which manifests that their capacitive measurements perform closely with no influence by loading  $\text{MnO}_2$  in the initial test. In the high frequencies,  $R_E$  represents the intrinsic resistance of the electrode and the ionic resistance of the electrolyte located the same measurement (inset of Fig. 5e). The semicircle region in the middle section corresponds to  $R_{CT}$ . The  $R_{CT}$  of the electrode material refers to the span of the semicircle arc. The span of the arc of the  $\text{MnO}_2$ -CNTs-CFC electrode increases after forested  $\text{MnO}_2$  with inferior electronic conductivity (Fig. 5e). It is from the EIS Nyquist plots that the low contact resistance of  $\text{MnO}_2$ -CNTs-CFC electrode was achieved (Fig. 5e) due to a large number of electronic conductive paths from CNTs and carbon fibers for charge transportation.

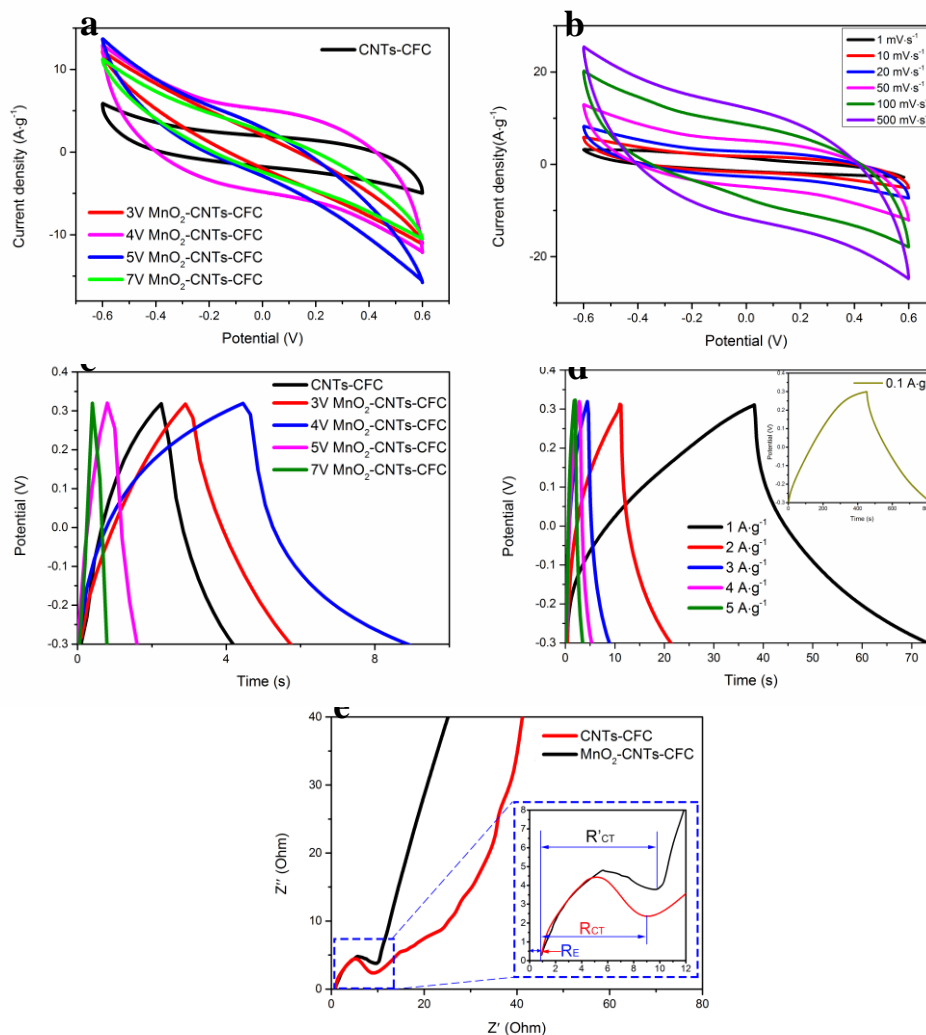


**Figure 5.** (a) Comparison of CV curves of CNTs-CFC and MnO<sub>2</sub>-CNTs-CFC at the scan rate of 50 mV·s<sup>-1</sup> (b) CV curves of MnO<sub>2</sub>-CNTs-CFC with 4V EPD voltage at various scan rates ranging from 1 mV·s<sup>-1</sup> to 500 mV·s<sup>-1</sup>, respectively (c) Comparison of galvanostatic charge-discharge curves of CNTs-CFC and MnO<sub>2</sub>-CNT-CFC with the different EPD voltages at a current density of 3 A·g<sup>-1</sup> (d) Galvanostatic charge-discharge curves of MnO<sub>2</sub>-CNT-CFC fabricated at 4V EPD voltage and (e) Nyquist plots.

Furthermore, stable cycling performance was obtained, which achieved a capacitance retention of 85 % with 1000 Charging-discharging cycles at the scan rate of 500 mV·s<sup>-1</sup> (Fig. 6a). Fig. 6b exhibits that the capacitance retention curves of MnO<sub>2</sub>-CNTs-CFC hybrid at various flexibility (bending, rolling, twisting) and release of foldability (1-, 2-, 3-times) states after 1000 charging-discharging cycles at the scan rate of 500 mV·s<sup>-1</sup>, respectively. Clearly, the profiles of curves during the course of the cycling kept the similar shape and showed no significant degradation. Moreover, as the folded times increase, the values of the capacitance retention of MnO<sub>2</sub>-CNTs-CFC decreases slowly. The superior rate capability in the MnO<sub>2</sub>-CNTs-CFC electrode could credit with the pine needle-shaped MnO<sub>2</sub>, which eases the volume expansion effect and enhances the cycling stability. The needle-shaped MnO<sub>2</sub> with nanosize effect provides enough space (Fig. 7) between adjacent nanoneedles to accommodate for volume change that’s associated with both charging and discharging.

The robust electrical contact was maintained due to that The needle-shaped  $\text{MnO}_2$  is electrically connected to the CNTs network as the current collector; furthermore, such an architecture enables all needle-shaped  $\text{MnO}_2$  to contribute to the capacity. The nanostructured needle-shaped  $\text{MnO}_2$  is more resistant to fracture than larger  $\text{MnO}_2$  structures because the insufficient total elastic energy stored in a small nanostructure during deformation due to initiate crack propagation. For smaller structures, the stress-relief volume that accompanies crack growth is insignificant compensate for the surface energy penalty associated with the crack growth. The needle-shaped  $\text{MnO}_2$  appeared to remain in contact with the CNTs conductive network, indicating minimal capacity fade because of the electrically disconnected material while cycling [40].

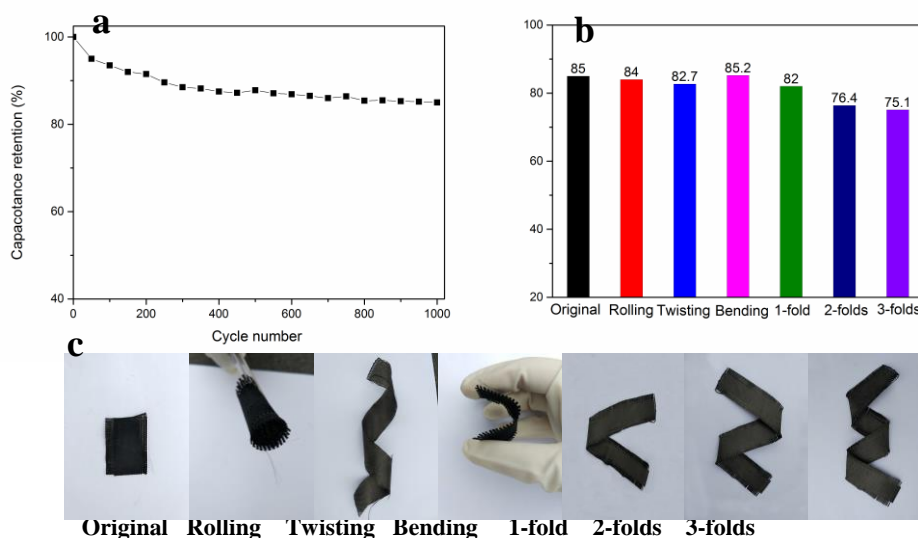


**Figure 6.** (a) Cyclic stability of  $\text{MnO}_2$ -CNTs-CFC hybrid at  $500 \text{ mV}\cdot\text{s}^{-1}$  (b) Comparison of the capacitance retention ratio as various states for  $\text{MnO}_2$ -CNTs-CFC hybrid at  $500 \text{ mV}\cdot\text{s}^{-1}$  for 1000 cycles(c) Digital photos illustrating the various states.

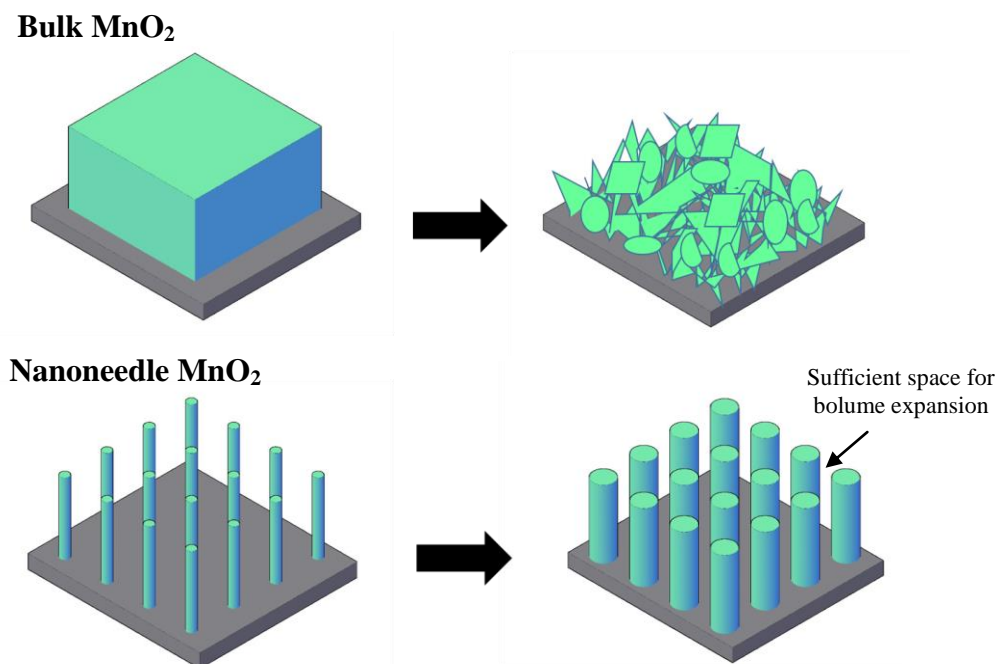


**Figure 7.** Schematic of nanosize effect for long cycling stability.

To further prove the good electrochemical performance of the as-prepared electrodes, our work has been compared with some published work. It can be seen from table 1 [41-45] that our work shows a good capacity. Compared with the published work, the cost of our work is low, the procedure is simple and the capacity is higher.

**Table 1.** The comparison of different electrode materials

Electrode material	Capacity	Procedure	Reference
RGO-AuNPs	288 F/g	Simple	41
Activated Carbon @ MnO <sub>2</sub>	221.45F/g	Simple	42
Cage-like Co <sub>3</sub> O <sub>4</sub>	642 F/g	Hard	43
MWCNTS/cobalt oxide	45.79 F/g	Simple	44
MWCNTs/iron oxide	64.74 F/g	Simple	44
Porous MnO <sub>2</sub>	452 F/g	Hard	45
MnO <sub>2</sub> /CNTs/Carbon cloth	381.74 F/g	Simple	Our work

#### 4. CONCLUSIONS

Bio-inspired hierarchical pine needle-shaped MnO<sub>2</sub>-CNTs-CFC composite was prepared by an environmentally-friendly two-step electrophoretic deposition (EPD) method. CNTs distributing uniformly on CFC are advantageous to increase the growth density of MnO<sub>2</sub>. The EPD for MnO<sub>2</sub> synthesis is easy to control the morphology of MnO<sub>2</sub>. Pine needle-shaped MnO<sub>2</sub> forests CNTs and more contact area can be obtained. Owing to the excellent electrical conductivity (both CFC and CNTs), large surface area of CNTs and high pseudocapacitance of MnO<sub>2</sub> with the shape pine of needle, it exhibits pleasurable specific capacitance of 381.74 F·g<sup>-1</sup>, promising energy density of 35.6 Wh·kg<sup>-1</sup> at scan of 1mV·s<sup>-1</sup> and 85% specific capacitance retained after 1000 cycles at scan of 500 mV·s<sup>-1</sup>.

#### ACKNOWLEDGEMENTS

This work has been supported by the fund of the State Key Laboratory of Solidification Processing in NWP (SKLSP201637), research fund of Shaanxi Provincial Department of Education (15JK1300 and 16JK1338) and the Ph.D. start-up fund of XPU (BS1501, BS1612 and BS1616).

#### References

1. G. Wang, Y. Ling, F. Qian, X. Yang, X. Liu and Y. Li, *J. Power Sources*, 196 (2011) 5209.
2. P. Thounthong, V. Chunkag, P. Sethakul, B. Davat and M. Hinaje, *IEEE Trans. Veh. Technol.*, 58 (2009) 3892.
3. P. Thounthong, V. Chunkag, P. Sethakul, S. Sikkabut, S. Pierfederici and B. Davat, *J. Power Sources*, 196 (2011) 313.
4. C. Xiong, T. Li, A. Dang, T. Zhao, H. Li and H. Lv, *J. Power Sources*, 306 (2016) 602.
5. X. Pu, M. Liu, L. Li, S. Han, X. Li, C. Jiang, C. Du, J. Luo, W. Hu and Z. Wang, *Adv. Energy*

- Mater.*, 6 (2016) 1601254.
6. Y. Xu, Y. Zhao, Y. Zhang, J. Ren Y. Zhang and H. Peng, *Angew. Chem. Int. Edit.*, 128 (2016) 8111.
  7. X. Lu, Z. Zhang, X. Sun, P. Chen, J. Zhang, H. Guo, Z. Shao and H. Peng, *Chem. Sci.*, 7 (2016) 5113.
  8. Z. Pan, J. Ren, G. Guan, X. Fang, B. Wang, S. Doo, I. Son, X. Huang and H. Peng, *Adv. Energy Mater.*, 6 (2016) 1600271.
  9. W. Weng, P. Chen, S. He, X. Sun and H. Peng, *Angew. Chem. Int. Edit.* 55 (2016) 6140.
  10. L. Liu, J. Pan. P. Chen, J. Zhang, X. Yu, X. Ding, B. Wang, X. Sun and H. Peng, *J. Mater. Chem. A*, 4 (2016) 6077.
  11. X. Cheng, X. Fang, P. Chen, S. Doo, I. Son, X. Huang, Y. Zhang, W. Weng, Z. Zhang, J. Deng, X. Sun and H. Peng, *J. Mater. Chem. A*, 3 (2015) 19304.
  12. X. Cheng, J. Zhang, J. Ren, N. Liu, P. Chen, Y. Zhang, J. Deng, Y. Wang and H. Peng, *J. Phys. Chem. C*, 120 (2016) 9685.
  13. Y. Zhang, Y. Zhao, X. Cheng, W. Weng, J. Ren, X. Fang, Y. Jiang, P. Chen, Z. Zhang, Y. Wang and H. Peng, *Angew. Chem. Int. Edit.*, 54 (2015) 11177.
  14. X. Zhao, B.M. Sanchez, P.J. Dobson, P.S. Grant, *Nanoscale*, 3 (2011) 839.
  15. P. Suktha, P. Chiochan, P. Iamprasertkun, J. Wutthiprom, N. Phattharasupakun, M. Suksomboon, T. Kaewsongpol, P. Sirisinudomkit, T. Pettong and M. Sawangphruk, *Electrochim. Acta*, 176 (2015) 504.
  16. Y. Cheng, S. Lu, H. Zhang, C.V. Varanasi and J. Liu, *Nano Lett.*, 12 (2012) 4206.
  17. Z. Fan, J. Yan, L. Zhi, Q. Zhang, T. Wei, J. Feng, M. Zhang, W. Qian and F. Wei, *Adv. Mater.*, 22 (2010) 3723.
  18. H. Xia, M. Lai and L. Lu, *J. Mater. Chem.*, 20 (2010) 6896.
  19. X. Zhao, B.M. Sanchez, P.J. Dobson and P.S. Grant, *Nanoscale*, 3 (2011) 839.
  20. C.L. Liu, K.H. Chang, C.C. Hu and W.C. Wen, *J. Power Sources*, 217 (2012) 184.
  21. J. Yan, T. Wei, B. Shao, Z. Fan, W. Qian, M. Zhang and F. Wei, *Carbon*, 48 (2010) 487.
  22. J. Wang, D. Jin, R. Zhou, X. Li, X. Liu, C. Shen, K. Xie, B. Li, F. Kang and B. Wei, *ACS Nano*, 10 (2016) 6227.
  23. G.A. Snook, P. Kao and A.S. Best, *J. Power Sources*, 196 (2011) 1.
  24. H.C. Hsu, C.H. Wang, S.K. Nataraj, H.C. Huang, H.Y. Du, S.T. Chang, L.C. Chen and K.H. Chen, *Diam. Relat. Mater.*, 25 (2012) 176.
  25. C. Yang, J. Shen, C. Wang, H. Fei, H. Bao and G. Wang, *J. Mater. Chem. A*, 2 (2014) 1458.
  26. X. Jiang, Y. Cao, P. Li, J. Wei, K. Wang, D. Wu and H. Zhu, *Mater. Lett.*, 140 (2015) 43.
  27. Y. Li, L. Guo, Q. Song, L. Li, K. Li, J. Lu and H. Li. *Ceramic Int.*, 41 (2015) 1943.
  28. Y. Li, L. Guo, Q. Song, H. Li, Q. Fu and K. Li. *J. alloy Compd.*, 636 (2015) 165.
  29. K.W. Nam and K.B. Kim, *J. Electrochem. Soc.*, 149 (2002) A346.
  30. L. Zhang and X.S. Zhao, *Chem. Soc. Rev.*, 38 (2009) 2520.
  31. S.B. Ma, K.Y. Ahn, E.S. Lee, K.H. Oh and K.B. Kim, *Carbon*, 45 (2007) 375.
  32. S.J. Campbell, D.C. Kelly and T.E. Peacock, *Aust. J. Chem.*, 42 (1989) 479.
  33. A. Ogata, S. Komaba, R. Baddour-Hadjean, J.P. Pereira-Ramos and N. Kumagai, *Electrochim. Acta*, 53 (2008) 3084.
  34. W. Chen, R.B. Rakhi, L.B. Hu, X. Xie, Y. Cui and H.N. Alshareef, *Nano Lett.*, 11 (2011) 5165.
  35. L. Feng, R. Wang, Y. Shi, H. Wang, J. Yang, J. Zhu, Y. Chen and N. Yuan, *Int. J. Electrochem. Sci.*, 11 (2016) 5962.
  36. B. Yuan, J. Zhang, R. Zhang, H. Shi, X. Guo, Y. Guo, X. Guo, S. Cai and D. Zhang, *Int. J. Electrochem. Sci.*, 10 (2015) 4899.
  37. D. Hu, B. Lu, K. Zhang, X. Sun, J. Xu, X. Duan, L. Dong, H. Sun, X. Zu and S. Zhen, *Int. J. Electrochem. Sci.*, 10 (2015) 3065.
  38. L. Liu, M. An, P. Yang and J. Zhang, *Int. J. Electrochem. Sci.*, 10 (2015) 1582.

39. B. Jugovi, B. Grgur, M. Antov, K.J. Zorica, J. Stevanovic and M. Gvozdenovic, *Int. J. Electrochem. Sci.*, 11 (2016) 1152.
40. W. Hui and C. Yi, *Nano Today*, 7 (2012) 414.
41. Z. Yu, S. Sun and M. Huang, *Int. J. Electrochem. Sci.*, 11 (2016) 3643.
42. T. Huang, Z. Qiu, D. Wu and Z. Hu, *Int. J. Electrochem. Sci.*, 10 (2015) 6312.
43. Y. Liang, Y. Yang, Z. Hu, Y. Zhang, Z. Li, N. An and H. Wu, *Int. J. Electrochem. Sci.*, 11 (2016) 4092.
44. A.S. Adekunle, K.I. Ozoemena, J.N. Lekitima, B.O. Agboola, E.E. Ebenso, J.A.O. Oyenkunle and O. S. Oluwatobi, *Int. J. Electrochem. Sci.*, 10 (2015) 3414.
45. C. Wan, L. Yuan and H. Shen. *Int. J. Electrochem. Sci.*, 9 (2014) 4024.

© 2017 The Authors. Published by ESG ([www.electrochemsci.org](http://www.electrochemsci.org)). This article is an open access article distributed under the terms and conditions of the Creative Commons Attribution license (<http://creativecommons.org/licenses/by/4.0/>).